PCCP

PAPER

Check for updates

Cite this: *Phys. Chem. Chem. Phys.*, 2018, **20**, 6845

Transport and accumulation of plasma generated species in aqueous solution†

C. C. W. Verlackt, * W. Van Boxem and A. Bogaerts *

Received 10th November 2017,
Accepted 6th February 2018

DOI: 10.1039/c7cp07593f

rsc.li/pccp

The interaction between cold atmospheric pressure plasma and liquids is receiving increasing attention for various applications. In particular, the use of plasma-treated liquids (PTL) for biomedical applications is of growing importance, in particular for sterilization and cancer treatment. However, insight into the underlying mechanisms of plasma–liquid interactions is still scarce. Here, we present a 2D fluid dynamics model for the interaction between a plasma jet and liquid water. Our results indicate that the formed reactive species originate from either the gas phase (with further solvation) or are formed at the liquid interface. A clear increase in the aqueous density of H_2O_2, HNO_2/NO_2^- and NO_3^- is observed as a function of time, while the densities of O_3, HO_2/O_2^- and $ONOOH/ONOO^-$ are found to quickly reach a maximum due to chemical reactions in solution. The trends observed in our model correlate well with experimental observations from the literature.

Introduction

The use of cold atmospheric plasmas (CAPs) for medical applications has grown into a large research field, attracting ever-growing interest in various scientific disciplines. Among these applications are the use of CAPs for wound healing,[1,2] sterilization,[3,4] blood coagulation[5,6] and even cancer treatment.[7,8] Indeed, reactive species generated by CAPs (*i.e.*, reactive oxygen and nitrogen species) can affect the signaling pathways inside treated cells, which influences their biological activity, inducing either cell proliferation or apoptosis.[9] A multitude of CAP sources, specifically to be used in biomedical applications, have been developed in the past decades by various research groups worldwide.[10–14] Among these sources are dielectric barrier discharges (DBDs) and the so-called floating-electrode DBDs, atmospheric pressure plasma jets (APPJs), including microscale APPJs, and the so-called plasma needle. As a result, a wide variety of setups, parameters and conditions are available for biomedical applications. Additionally, a distinction can be made between direct and indirect treatment. In direct treatment, the treated (biological) substrate forms an active part of the plasma discharge, *e.g.*, playing a role as a counter-electrode in the case of a DBD. On the other hand, in indirect treatment, the plasma discharge does not come in contact with the treated substrate, *e.g.*, when the plasma plume of a jet does not reach the substrate.

Recently, a novel approach for biomedical plasma treatment has been introduced and became the subject of increasing investigation:[15–17] the use of Plasma Treated Liquids (PTL), often also called Plasma Activated Liquids (PAL) or Plasma Activated Water (PAW), or (the quite popular term) Plasma Activated Media (PAM). Indeed, several different terms are used in the literature, denoting liquids processed by plasma, but because of the absence of an established terminology, we will use the term PTL in this work. Using PTL, biological substrates are treated with a liquid that has been in contact with a plasma source prior to the biomedical application. In this way, the plasma generated species are induced in a liquid. This liquid is then used to transport these (usually more long-lived) plasma-induced chemicals to the biological substrate. This enables a more homogeneous treatment of the tissue and the ability to store the plasma activity.[17] In this way, plasma treatment can be assured even at moments or at places where no plasma source is available. Furthermore, the substrate only comes in contact with liquid-soluble and long-lived reactive oxygen and nitrogen species (RONS) such as H_2O_2, HNO_2 and HNO_3, eliminating the effects of the plasma generated radicals and UV radiation. Finally, PTL can be injected inside the tissue whereas direct CAP treatment transports RONS in the first few layers only[18,19] due to the often high reactivity and the short half-live of most plasma species.[20]

In literature, a variety of different liquids have been used to generate PTLs, ranging from pure water and buffered solutions to complex biomedical media.[15,21–24] The choice of liquid greatly influences the resulting PTL in terms of the concentration of species, acidity, *etc.*[21] In a recent study, performed in collaboration with the Ruhr Universität Bochum, we reported

Research group PLASMANT, University of Antwerp, Department of Chemistry, Universiteitsplein 1, 2610 Wilrijk, Belgium.
E-mail: Christof.verlackt@uantwerpen.be, Annemie.bogaerts@uantwerpen.be

† Electronic supplementary information (ESI) available. See DOI: 10.1039/c7cp07593f

that the plasma treatment of non-buffered water results in a noticeable decrease in pH.[25] This was countered by using buffered solutions such as PBS (Phosphate Buffered Saline). Additionally, aqueous liquids often contain ions like Cl^-, which in an oxidative environment forms hypochlorous acid (HOCl), showing strong antibacterial activity.[26] Being a reactive species, HOCl is known to interact and react not only with biomolecules, such as DNA and proteins, but also with other reactive species in solution, like H_2O_2 and O_2^-, influencing the plasma chemistry in the liquid.[27–29]

In addition, a wide range of biological media can also be used, leading to the creation of Plasma Treated Media (PTM) or PAM (see above). Note that PTM differs significantly from (buffered) plasma treated water (PTW) as several additional long-lived reactive species can be generated, such as amino acid peroxides. This offers a new dimension for biomedical applications as these biochemical reactive species (often having a longer life-time than most RONS) can migrate to cells which are far away from the treated area.[22,30–33] Moreover, the presence of certain amino acids (*i.e.*, phenylalanine, alanine, histidine, arginine, tyrosine, and lysine) has proven to enhance the anti-tumor activity of PTM.[22] However, this also limits the storage of RONS in PTM as they will be constantly involved in reactions with the biomolecules present in the medium.[17]

Although the confidence for the applicability and added value of PTLs in plasma medicine is clearly increasing,[34–39] insight into the fundamental mechanisms of the generation of reactive species and in the activity of PTLs is still lagging.[40] While experiments can provide useful information, computational approaches can also be of great value, and are ideally suited to provide answers to the open questions. Babaeva and Kushner[41] computationally investigated the interaction between DBD plasma filaments and dry wounds.[41] This was expanded by introducing a liquid layer in a 0D model[42] to investigate the interaction and penetration of the electric fields on liquid covered wounds. Chen *et al.*[43] used a 0D model to evaluate the plasma–liquid chemistry for a He/O_2 DBD using a set of 21 plasma species and 267 reactions,[43] in the framework of treating biofilms and biological tissues. In addition, Suda *et al.*[44] presented a 0D model for a He/N_2 DBD, investigating the effect of the gap on the surface voltage as well as the accumulation of plasma species in a liquid layer.[44] They used a model containing 10 species and 20 reactions. Another important computational study on the interactions of DBD with a liquid layer was performed by Tian and Kushner.[45] They presented a 2D fluid model for the accumulation of reactive species in the liquid. The obtained knowledge was extended by Lietz and Kushner,[46] who used a 0D model to gain more detailed insight into the plasma–liquid chemistry when treating liquid covered tissue with a DBD. Finally, Liu and coworkers[47,48] provided interesting insight into the propagation of reactive species in the liquid phase and investigated the effect of the gap on the simulated plasma chemistry.[47,48] For this purpose, they used an extensive 0D model containing 53 RONS and 624 reactions to calculate the chemistry both in the gas and liquid phases.

The above studies all focus on the interaction of DBD plasma with a liquid. However, only a few papers report on modeling the interactions between a plasma jet and a liquid surface. Norberg *et al.*[49] investigated the impact of the operating voltage on the generation and accumulation of reactive species in a liquid layer using a 2D model for a He plasma jet.[49] This study provided insight into the difference between direct (touching) and indirect (non-touching) treatment of a liquid layer using a plasma jet. In 2016, the authors expanded their model with the aim of elucidating the delivery of an electric field from an APPJ to liquid-covered tissue and again evaluated the effect of the voltage on the calculated system.[50] Finally, essential understanding in the accumulation of species in the liquid layer was obtained by Lindsay and Graves.[51] They investigated the transport of a limited number of reactive species produced by a He plasma jet to liquid water, using a 2D model containing 13 species and 23 reactions.

In this work, we present a 2D axisymmetric fluid model to investigate both the accumulation and reactivity of biologically relevant reactive species in a buffered aqueous solution during the treatment with an Ar plasma jet, based on the kINPen, flowing in ambient air (78.09% N_2, 20.95% O_2 and 0.96% H_2O). This plasma jet is widely used in experiments,[1,52–56] and even in clinical studies,[57–59] but its interaction with a liquid has not been described in a two-dimensional model system before. A photograph of the kINPen plasma jet is presented in Fig. 1. We focus especially on the biologically relevant species. In total, 20 gaseous and 22 aqueous species are included, as well as 57 and 42 reactions in the gas and liquid phases, respectively.[56,60] Using an Ar plasma jet with a flow rate of 3 slm, we expect high gas velocities,[61] which will have a tremendous impact on convection, and therefore on the plasma chemistry in both the gas and the liquid. Therefore, we focus especially on these effects, providing information on the accumulation and reactivity of reactive species in the liquid phase during treatment.

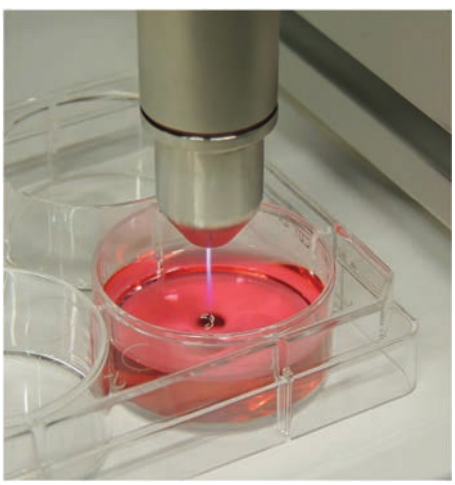

Fig. 1 Photograph of the kINPen IND plasma jet, as used during the treatment of liquids.

This journal is © the Owner Societies 2018

Results and discussion

Flow behavior of the gas and liquid phase

As explained in the Computational setup, the first step in the investigation is to simulate both the gas and liquid flow, until a steady-state is reached. Subsequently, the gas and liquid flow velocities are introduced as input in the time-dependent model. Fig. 2 illustrates the steady-state gas and liquid flow behavior, for an inlet gas flow rate of 3 slm Ar in the geometry. The color map in Fig. 2 illustrates the velocity magnitudes in both gas and liquid phases, while the velocity directions are depicted with arrows. This inlet gas flow rate of 3 slm yields an average gas velocity of 26.1 m s^{-1} in the afterglow, as is clear from Fig. 2. This is in agreement with calculated values reported in the literature, for the same plasma jet diameter of 1.6 mm.[56,66] The gas that exits the nozzle will reach the interface (height of 0 cm) and subsequently flow along the interface outwards, inducing shear stress on the liquid. Because of this, the upper liquid layer (thickness of 200 μm) will also start to flow in the same direction as the gas flow, with a maximum velocity of 10.4 m s^{-1}. This liquid flow leads to the formation of a reverse vortex near the border of the liquid vessel. A close-up of this reverse vortex is presented at the right side in Fig. 2. Furthermore, when reaching the border of the liquid vessel (at radius = 3.5 cm), the velocity in the liquid is greatly reduced within the reverse vortex (to a maximum value of 0.54 m s^{-1}).

Due to the presence of this reverse vortex, the liquid (at a depth of 200 μm and lower) will start flowing back towards the center, in the opposite direction compared to the liquid flow at the interface. When reaching the center of the vessel, the flow is subsequently guided towards the bulk of the liquid (*cf.* Fig. 2). This results in an interesting flow pattern in the liquid which, at first sight, seems to contradict some experimentally observed flow patterns.[63,64] However, the depth at which the liquid flows in the opposite direction from the flow at the interface greatly depends on the velocity of the gas that flows along the interface, and thus on the gas flow rate. At 3 slm, this opposite flow in the liquid phase occurs at a depth of *ca.* 200 μm, while it is roughly at 300 μm for 2 slm and 400 μm for 1 slm. This is illustrated in Fig. 3 for these three different flow rates. Note that the color codes of the gas flow and liquid flow are the same in this figure, to indicate that the liquid velocity at the interface is equal to that of the gas flow. The observations reported by Hefny, *et al.*[64] are obtained at helium flow rates of 1.4 slm and a gap of 4 mm, resulting in significantly lower gas velocities at the liquid interface, and this affects the flow pattern inside the liquid, as is clear from Fig. 3.

To illustrate this in more detail, we calculated the liquid flow pattern for an inlet Ar flow rate of 0.1 slm, yielding an average gas velocity of 0.7 m s^{-1} in the afterglow, and the result is presented in Fig. S1 in the ESI.† For a 0.1 slm Ar flow rate, we observe an almost identical liquid flow pattern as presented in the experimental paper of Hefny, *et al.*[64] Indeed, the reverse

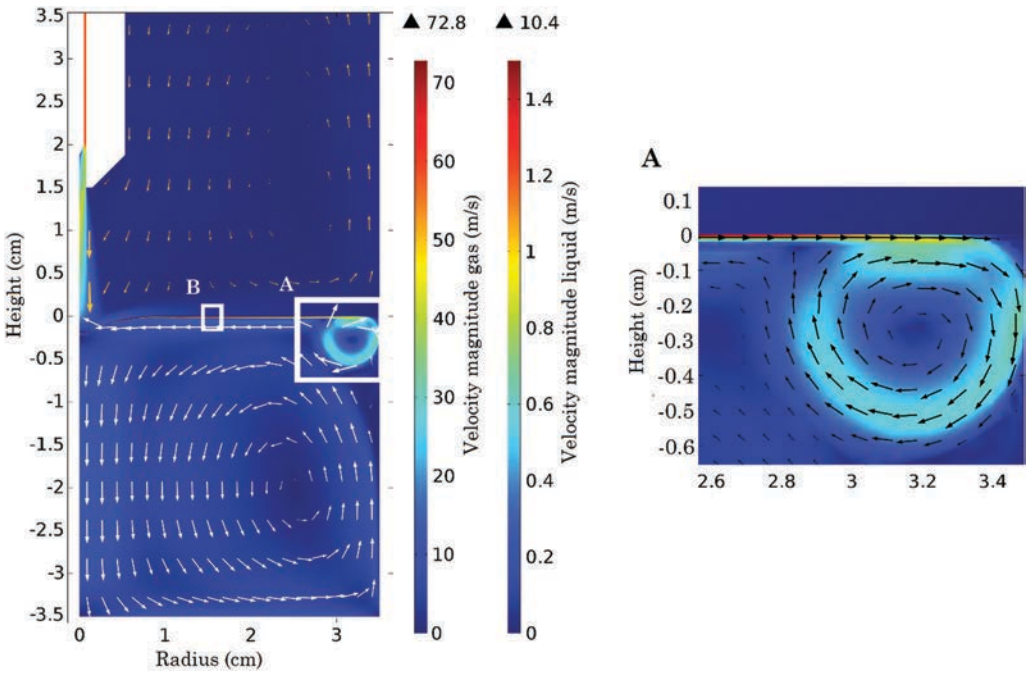

Fig. 2 2D plot of the velocity magnitude (depicted in a rainbow color scale) in both gas and liquid phase, at an inlet gas flow rate of 3 slm. The direction of the flow is indicated by yellow and white arrows for the gas and liquid phase, respectively. The arrows are logarithmically scaled based on the velocity magnitude, for the sake of clarity. The symmetry axis is located at radius = 0 cm. Given the vast difference between the liquid velocity at the interface and bulk, the color scale is shifted to lower values for the sake of clarity. The values above the color scale indicate the highest velocity in both gas and liquid phases (in m s^{-1}). A zoom of the 2D plot in the white box indicated with letter 'A' is presented on the right side of the figure. It shows a close-up of the reverse vortex in the liquid, located at the interface, using the same color scale as in the main figure. The arrows indicating the direction of the flow are depicted in black in the right figure. The white box indicated with letter 'B' represents the close-up used in Fig. 3.

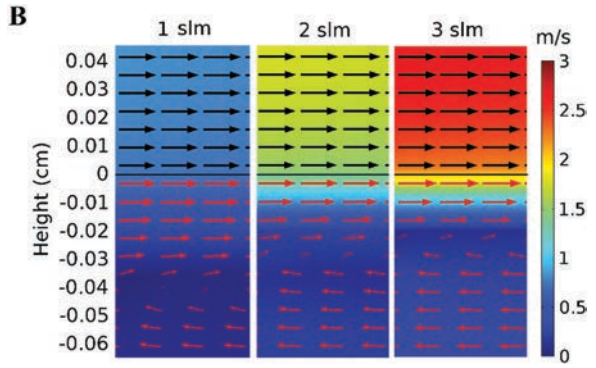

Fig. 3 Close-up of the interface (in the white box indicated by letter 'B' in Fig. 2) at three different inlet gas flow rates, *i.e.*, 1, 2 and 3 slm. The same color code is used for both the gas and liquid phases, to clearly indicate that the maximum liquid velocity is found in the top layers of the liquid, and is equal to the velocity of the gas at the interface. The arrows indicate the direction of the flow in the gas phase (black) and liquid phase (red). The gas–liquid interface (at a height of 0 cm) is indicated by a black line.

flow now reaches depths of around 1 cm, leading to an opposite flow pattern in the liquid bulk compared to the flow pattern in the case of 1, 2 and 3 slm of Ar (see Fig. 2 and 3 above). Thus, it is clear that a higher gas velocity forces the observed reverse vortex towards the interface and to the border of the liquid vessel (*cf.* Fig. 2).

Temperature profile in the gas and liquid phases

Using the steady-state velocity profiles presented above, we calculate the transport of heat and mass as a function of time, yielding the temperature and species concentration profiles. The temperature profiles in both the gas and the liquid, after 1 minute of plasma treatment, are presented in Fig. 4. As soon as the inlet gas (initially at 327 K) reaches the interface, it flows along the liquid surface outwards, as was illustrated in Fig. 2. The temperature of the gas quickly decreases once it comes into

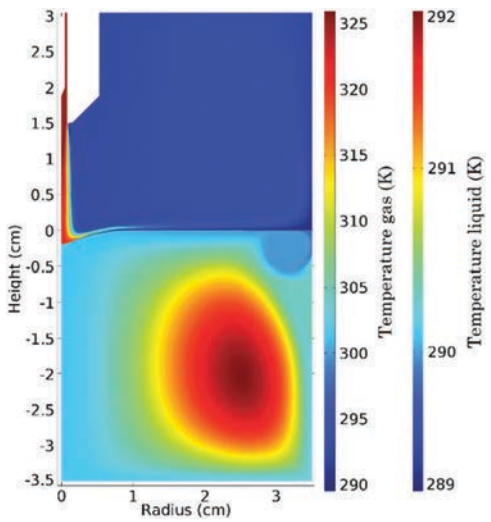

Fig. 4 2D plot of the temperature in both the gas and liquid phases after 1 minute of plasma treatment, presented in a rainbow scale.

contact with the liquid, reaching the liquid temperature. At the same time, the liquid temperature, which was initially 293 K, slightly decreases as a function of time, to an average of 291 K after 1 minute. Furthermore, the temperature of the liquid and gas at the interface is identical, reaching a minimum value of 289 K at the border of the liquid vessel and the reverse vortex (at radius = 3.5 cm in Fig. 4).

The drop in liquid temperature is a result of the evaporation of water due to convection and is consistent with the model predictions by Lindsay and Graves.[51] When the water vapor above the interface is blown away by the plasma jet, liquid water evaporates in order to maintain the equilibrium in vapor pressure. This evaporation process consumes heat, leading to some cooling of the liquid, as observed in Fig. 4. The slight drop in liquid temperature might be at first sight counter-intuitive, as the initial temperature of the gas is higher than that of the liquid, so we might expect a heating effect. To verify that the drop in liquid temperature by evaporation is more important than the eventual increase due to the higher gas temperature, we performed a calculation where the evaporation was disabled (see Fig. S2 in the ESI†).

It is clear from this figure that the liquid temperature now slightly increases (*i.e.*, less than 1 K after 1 min), indicating that the cooling effect of evaporation of the liquid is indeed stronger than the heating effect by the warm gas effluent. Note that our calculations were performed using a liquid volume of 135 mL, with an interface of 38.5 cm^2. Thus, the area of evaporation ($\approx$38.5 cm^2) is more than 100 times larger than the area where the warm effluent reaches the liquid ($\approx$0.28 cm^2), and thus, cooling of the liquid can indeed be expected.

Species concentrations in the gas phase

Fig. 5 shows the species number densities in the afterglow as a function of distance from the nozzle of the plasma jet device. The interface is located at 17 mm (15 mm gap + 2 mm depression). At the top of the figure, we included a timescale axis, which is obtained from the distance in combination with the local gas velocity of the effluent. This time-information is useful when interpreting the gas chemistry. A clear increase in densities of the long-lived species, *i.e.*, O_3, HNO_2, HNO_3, H_2O_2 and H_2 is observed, while the densities of the radicals, *i.e.*, OH, O, N, H and HO_2, show a steady decrease, indicating that they are consumed for the formation of the more long-lived species. NO appears to be an exception, as its density remains relatively constant, and it reaches the gas–liquid interface with a density of around 5×10^{13} cm^{-3}. The latter also explains the increase in NO_2 density, because the production of NO_2 mainly relies on the presence of NO in the effluent (through the reactions between NO and O, HO_2 or NO_3, see Table S2, ESI†). The trends in NO and NO_2 densities are in good agreement with the results of other plasma models,[56,61,69] indicating that NO is more stable than the other short-lived species and plays an active role in the production of NO_2. Indeed, the reaction rates for NO (both production and loss) are typically lower than the reaction rates for OH, O, N and HO_2. Thus, more time is needed for NO to be consumed, leading to a relatively high density of NO in

 This journal is © the Owner Societies 2018

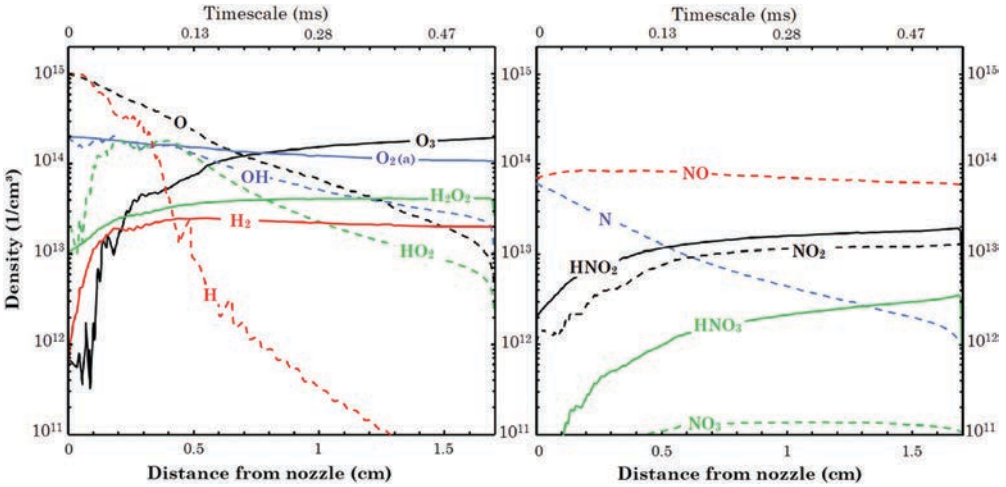

Fig. 5 Number densities of the reactive oxygen and nitrogen species (RONS) in the gas phase, after 1 min of plasma treatment. The species containing O and/or H are plotted in the left panel, while the reactive nitrogen species are plotted in the right panel. Radicals are indicated with dotted lines, while molecules are depicted using solid lines. The gas–liquid interface is located at 17 mm distance from the nozzle (15 mm gap + 2 mm depression). The densities of species with a high Henry's constant, such as H_2O_2 and OH, show a sudden drop at the interface due to the fast transfer to the liquid phase. The timescale indicated at the top axis is calculated from the distance and the local gas velocity.

the effluent (*cf.* Fig. 5). Although the comparison between 0D chemical kinetics models and fluid dynamics-kinetics models is difficult due to different assumptions and approximations, the observed trends in Fig. 5 are in good agreement with the density profiles as calculated by 0D simulations using similar input parameters.[61] This validates the reduced chemistry and confirms that the most important gas phase chemistry is included in our model.

Some species presented in Fig. 5 (*i.e.*, O_3, HO_2, OH and H) exhibit a non-smooth density profile. This is especially pronounced in the first 0.5 cm of the afterglow. There are two reasons for this behavior. First of all, it can be explained by the turbulent gas flow pattern found under the nozzle. Hence, the diffusion of ambient air components (*i.e.*, O_2, N_2 and H_2O) becomes more turbulent, and the species for which the production heavily relies on the concentration of the ambient air components, will show a non-smooth density profile as a function of distance. For instance, the production of O_3 in the afterglow, close to the nozzle, is controlled by reaction 2 of Table S2 (ESI†), leading to an increase in O_3 density at the side of the nozzle where the density of O_2 is high. This is shown in Fig. 6. However, the gas flow turbulence at the side of the nozzle is more pronounced as well, explaining the non-smooth profile for the O_3 density. A similar explanation can be given for the HO_2 density, which is mostly produced by reaction 40 of Table S2 (ESI†) close to the nozzle.

$$O + O_2 + M \rightarrow O_3 + M \quad (2)$$

$$H + O_2 + M \rightarrow HO_2 + M \quad (40)$$

In addition, the non-smooth density profile close to the nozzle can also be explained by the sharp boundary condition in our model, as chemical reactions only start when the species leave the nozzle. As the concentration of radicals, such as H and OH, is high at the nozzle (*cf.* Table S1 in the ESI†), these species start to react immediately, which can have a great impact on their densities in the first millimeters after the nozzle.

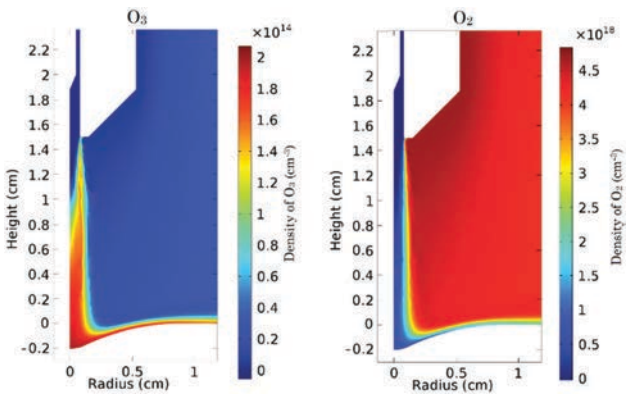

Fig. 6 2D plot of the number densities of O_3 (left) and O_2 (right) in the gas phase, after 1 min of plasma treatment, at a gas flow rate of 3 slm. The axis of symmetry is located at radius = 0 cm. The O_3 density increases sharply near the nozzle, where the concentration of O_2 is very high. As the gas flow is turbulent in this region, this will affect the density profile of O_3 when O atoms react with the ambient O_2 gas molecules (*cf.* reaction 2 of Table S2, ESI†). See also Fig. 5.

Transport of species in the liquid phase

At the gas–liquid interface (distance = 1.7 cm in Fig. 5), a sharp drop in the density of various species can be observed, *i.e.*, more specifically, those with a high Henry's constant, *i.e.*, H_2O_2, OH, O, HO_2, HNO_2, HNO_3 and NO_3 (*cf.* Table S3, ESI†). On the other hand, the densities of species with a low Henry's constant will remain constant above the gas–liquid interface. This behavior is shown in Fig. 7 for the 2D density profiles of H_2O_2 and O_3, which are characterized by a high and low Henry's constant, respectively.

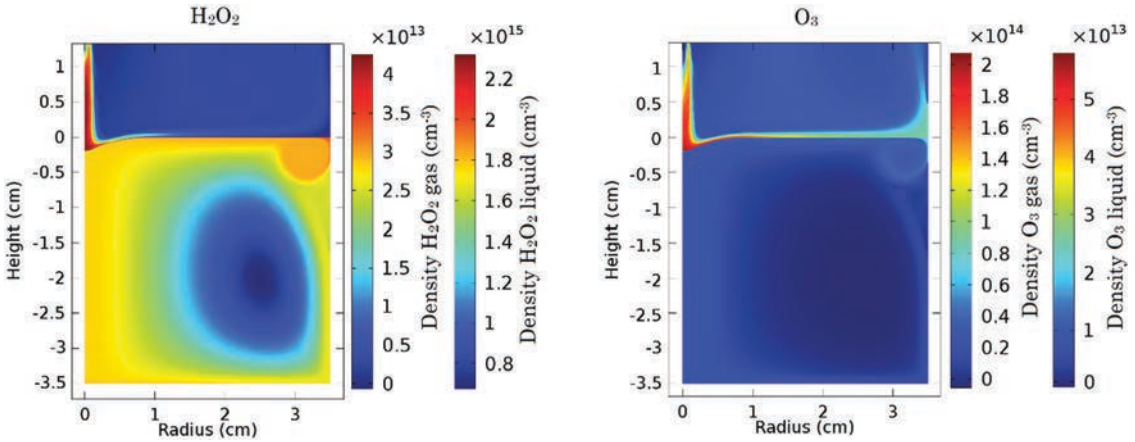

Fig. 7 2D plot of the number densities of H_2O_2 (left) and O_3 (right) in the gas phase just above the interface, as well as in the liquid, after 1 min of plasma treatment, at a flow rate of 3 slm. The axis of symmetry is located at radius = 0 cm. H_2O_2 has a Henry's constant of 7.9×10^4 leading to an accumulation in the liquid phase and a depletion in the gas phase (*cf.* Fig. 5). O_3 has a Henry's constant of 1.22×10^{-2} and will therefore accumulate in the gas phase just above the interface, leading to a much lower concentration in the liquid phase.

Once the gas species are in the liquid, they will be transported by both diffusion and convection. Due to the rather high velocity of the liquid at the interface (*cf.* Fig. 2), convection will contribute most to the transport of species in the liquid. This is also clear from Fig. 7, where the flow pattern in the liquid (*cf.* Fig. 2) is also clearly visible in the density profiles of the dissolved species. The importance of convection for the transport and accumulation of species in the bulk liquid was also demonstrated by Lindsay and Graves,[51] who reported a steady increase in the concentration of reactive species in the liquid, when convection was turned on.

Following the liquid flow as depicted in Fig. 2, the dissolved species will initially remain at the gas–liquid interface and will accumulate in the observed reverse vortex. They will also flow back along the top layers of the liquid, following the liquid flow, after which they are introduced in the bulk liquid (as seen in Fig. 7 left).

Species concentrations in the liquid phase

The 1D spatial density profiles of the reactive species in the liquid are presented in Fig. 8, *i.e.*, at a depth of 100 μm along the interface (Fig. 8A) and as a function of depth at the symmetry axis (Fig. 8B). Note that the plot in Fig. 8A only starts at r = 0.7 cm, due to the presence of the depression in the liquid.

The fast consumption of short-lived species, *i.e.*, OH, NO_2 and NO_3, in the liquid is obvious from Fig. 8A. Indeed, their densities drop with multiple orders of magnitude within 1 mm

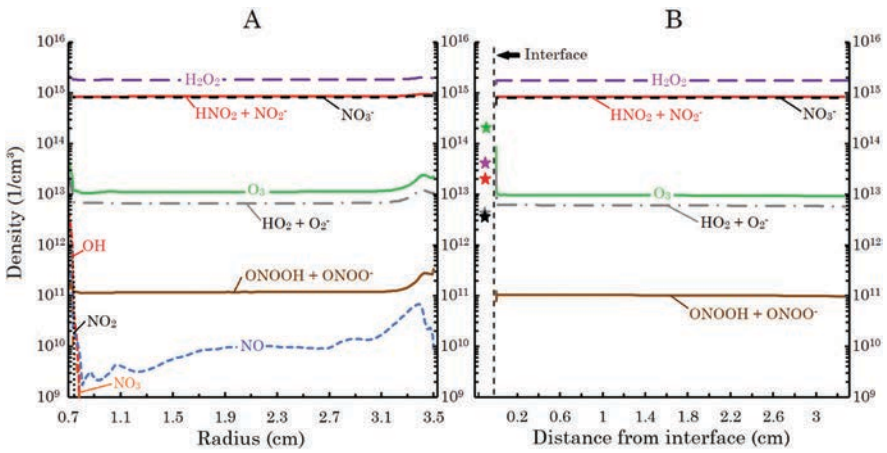

Fig. 8 Number densities of the reactive oxygen and nitrogen species (RONS) in the liquid, after 1 min of plasma treatment, at a flow rate of 3 slm. (A) Densities at a depth of 100 μm below the gas–liquid interfaces as a function of radial distance. The densities of OH, NO_2 and NO_3 decrease dramatically when introduced in the liquid. They are only present right below the interface, and only for about 1 mm in the radial direction. They do not exist in deeper layers, and are therefore not present in (B). (B) Densities along the symmetry axis (r = 0 cm) as a function of depth. The densities of the corresponding gas phase species above the interface are indicated by an asterisk, showing that the density of O_3 is much higher in the gas phase compared to the liquid phase (due to a low Henry's constant) while the opposite is true for H_2O_2, HNO_2 and HNO_3 (due to a high Henry's constant). The densities of gaseous HO_2 and HNO_3 are almost identical, so their asterisks overlap.

 This journal is © the Owner Societies 2018

along the interface, and they are completely consumed in the lower liquid layers to produce long-lived species (explaining why their densities are not plotted in Fig. 8B). This clearly demonstrates their importance in the liquid chemistry at the liquid depression (where the effluent interacts with the interface) and the first layers in the solution. On the other hand, the densities of the other species, *i.e.*, H_2O_2, HNO_2/NO_2^-, NO_3^-, HO_2/O_2^-, O_3 and $ONOOH/ONOO^-$, remain relatively constant as a function of distance, both in the horizontal and vertical direction. As the liquid needs roughly 0.2 seconds to reach 3.5 cm along the symmetry axis (*cf.* Fig. 8B), it can be concluded that the chemistry needs longer timescales to significantly affect the concentration of the long-lived species.

In Fig. 8B, the gas densities of the species that reach the bulk liquid are shown by an asterisk in the same color (taken at 1.65 cm below the nozzle, *i.e.*, before the sudden depletion, as presented in Fig. 5). Note that only the densities of the long-lived species are presented in this figure. The action of Henry's law is very clear, because species with a high Henry's constant, *i.e.*, H_2O_2, HNO_2 and HNO_3, are found at significantly higher densities in the liquid phase compared to their densities in the gas phase, while the opposite is true for O_3, which has a low Henry's constant. Moreover, the accumulation of the dissolved species at the reverse vortex is visible from Fig. 8A, showing an increase in the densities for all the reactive species at a radial distance of 3.4–3.5 cm. As mentioned, this is caused by the sudden decrease in liquid velocity and the recirculation inside this vortex, leading to an accumulation of the species.

Note that NO clearly accumulates in the reverse vortex, with densities almost comparable with some long-lived species, while it is immediately consumed in the bulk liquid. Indeed, NO is not found in Fig. 8B. The same is true for NO_3, which also accumulates in the reverse vortex, reaching a maximum density of 7.5×10^8 cm^{-3} at a radial position around 3.36 cm (not shown in Fig. 8, because of the too low density).

From Fig. 8B, it can be deduced that only H_2O_2, HNO_2/NO_2^-, NO_3^-, O_3, HO_2/O_2^- and $ONOOH/ONOO^-$ are able to enter the bulk liquid and accumulate in the solution. To obtain more insight into the accumulation of these species, we plot their number density, averaged over the entire liquid volume (135 mL) as a function of time in Fig. 9. It should be stressed that these accumulations are only calculated during plasma treatment and not after. After 1 minute of plasma treatment, H_2O_2 has the highest concentration (1.3×10^{15} cm^{-3}) in the solution, followed by NO_2^- and NO_3^- (6.3×10^{14} and 6.0×10^{14} cm^{-3}, respectively). The concentrations of these species increase monotonically as a function of time during plasma treatment, consistent with the results obtained from experimental studies.[70,71]

This increase, however, is not observed for the other species, which are found in much lower numbers. The concentration of O_2^- increases sharply in the first 10 seconds, and subsequently it reaches a constant value of around 2.6×10^{12} cm^{-3}. As HO_2 and O_2^- are connected through a pK_a value of 4.88, the same is true for HO_2, albeit at a significantly lower concentration. This is caused by the increasing importance of loss reactions 77 and 92 (see Table S2 in the ESI†), which eventually become equal to

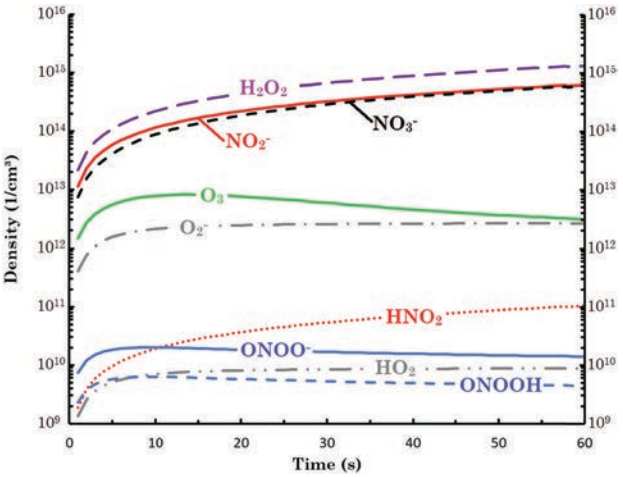

Fig. 9 Number densities of the reactive species that accumulate in the liquid, as a function of time. The number densities are averaged over the entire liquid volume (135 mL). The pH of the liquid was set at 7.3. As HNO_2, HO_2 and ONOOH are weak acids, both the neutral molecule and their conjugated base are presented in the figure.

the accumulation of HO_2/O_2^- (*via* solvation and production reactions), leading to a steady-state as observed in Fig. 9.

$$HO_2 + H_2O + O_2^- \rightarrow O_2 + H_2O_2 + OH^- \quad (77)$$

$$HO_2 + HO_2 \rightarrow O_2 + H_2O_2 \quad (92)$$

The concentration of O_3 also increases steeply, reaching a maximum value of 8.1×10^{13} cm^{-3} after 14 seconds, but it declines steadily afterwards. This is the result of an important loss reaction (reaction 70 in Table S2, ESI†), which is affected by the increasing concentration of NO_2^-, consistent with the work of Lukès *et al.*[70]

$$NO_2^- + O_3 \rightarrow O_2 + NO_3^- \quad (70)$$

A similar trend is also found for $ONOOH/ONOO^-$, but the reason is less trivial. Within the solution, the production of $ONOOH/ONOO^-$ is mainly controlled by reactions 83 and 84 of Table S2 (ESI†), and thus it depends on the concentration of short-lived species like OH, HO_2 and NO.

$$NO + HO_2 \rightarrow HOONO \quad (83)$$

$$NO_2 + OH \rightarrow 0.7(NO_3^- + H^+) + 0.3(ONOOH) \quad (84)$$

Therefore, the production of $ONOOH/ONOO^-$ mainly takes place just beneath the gas–liquid interface, where these species still have a reasonable density. However, the concentrations of other long-lived species, such as H_2O_2 and NO_2^-, just beneath the interface will also increase, due to recirculation in the liquid (*cf.* Fig. 2). Because of this, the short-lived species, necessary to produce $ONOOH/ONOO^-$, will also be consumed by reactions with these long-lived species, thus decreasing the production rates of $ONOOH/ONOO^-$. Combined with the fact that $ONOOH/ONOO^-$ decomposes again in water into short-lived species, such as OH, NO, O_2^- and NO_2 (reactions 89–91 in Table S2, ESI†), this explains the drop in the concentration of

$ONOOH/ONOO^-$ as a function of time. In the bulk liquid, the production of $ONOOH/ONOO^-$ is governed by the reaction between H_2O_2 and NO_2^- (reaction 78 in Table S2, ESI†). However, this process is much slower compared to the reactions with short-lived species as observed in the interface, and will therefore only have a small contribution to the production of $ONOOH/ONOO^-$ during plasma treatment.

Thus, from Fig. 9, we can expect that only H_2O_2, HNO_2/NO_2^- and NO_3^- will remain in the solution after treatment, while O_3, HO_2/O_2^- and $ONOOH/ONOO^-$ will be consumed, due to faster loss rates compared with production rates.

$$H_2O_2 + NO_2^- + H^+ \rightarrow ONOOH + H_2O \quad (78)$$

$$ONOOH \rightarrow NO_3^- + H^+ \quad (89)$$

$$ONOOH \rightarrow OH + NO_2 \quad (90)$$

$$ONOO^- \rightarrow NO + O_2^- \quad (91)$$

Overview of the liquid chemistry

Finally, we investigate the most important chemistry in the liquid phase, paying special attention to the differences between the bulk liquid and the initial layers just beneath the gas–liquid interface around the depression in the liquid (called here "liquid interface" for the sake of clarity). An overview is presented in Fig. 8. It starts from the gas phase species that (i) interact with the liquid interface (*cf.* Fig. 5), and (ii) play a role in the liquid chemistry (*cf.* Fig. 8 and Table S2, ESI†). We focus especially on the species with the highest densities in Fig. 9, *i.e.*, H_2O_2, HNO_2/NO_2^-, NO_3^-, O_3, HO_2/O_2^- and $ONOOH/ONOO^-$. The species are written in boxes of which the thickness is a measure for the species relative density in that specific phase (bold being the highest density, such as O_3 in the gas phase, and dashed being the lowest, such as NO_3 in the gas phase). In this figure, reactions with ambient gas molecules (N_2, O_2 and H_2O) are included, but these species are not depicted for the sake of clarity.

As shown in Fig. 5, O_3 reaches the gas–liquid interface with the highest density of all RONS, followed by NO, H_2O_2, and HNO_2. This is indicated by the thickness of the boxes of these species in the gas phase in Fig. 10. Note that H_2 also reaches the gas–liquid interface with relatively high density (*cf.* Fig. 5), but as it is not involved in the reactions that provide a significant contribution to the liquid phase species, it is not included in Fig. 10. The same applies for O_2(a), which is not included in the liquid phase chemistry, because of a lack of data (see discussion Computational setup). The transfer of species from one phase to the other is represented by vertical blue arrow lines in Fig. 10, and the thickness of the arrow line is a measure for the fraction of that species that reaches its destination. For instance, H_2O_2 and HNO_2 can easily enter the liquid due to their high Henry's constant, so the blue arrow line is thick compared to that of O_3, which has a low Henry's constant. Indeed, despite the high density of O_3 and NO above the liquid interface (*cf.* Fig. 5), only a small fraction is able to enter the liquid due to their low Henry's constant, leading to liquid densities that do not exceed the order of 10^{13} cm^{-3} in

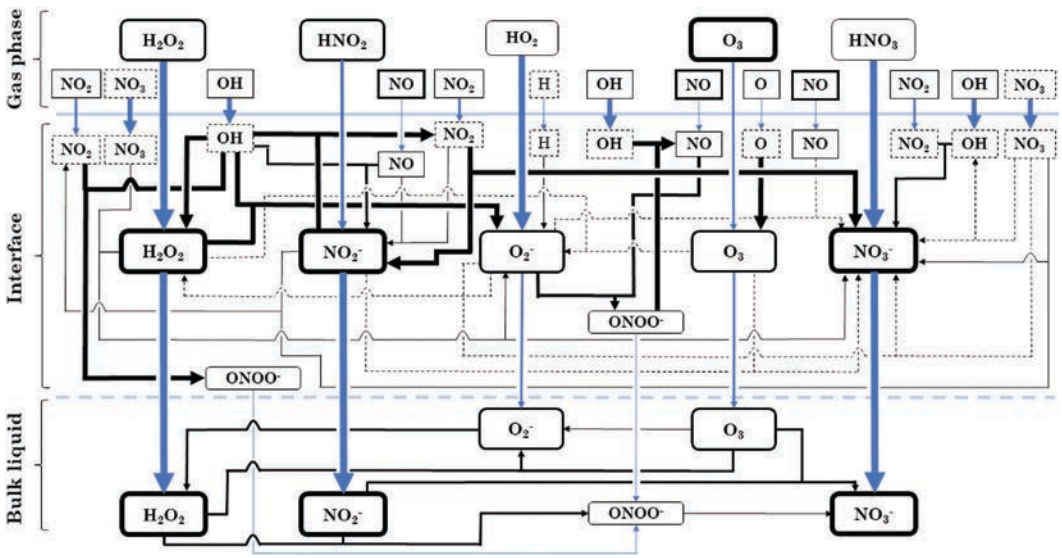

Fig. 10 Reaction diagram of the observed liquid chemistry. The diagram mainly focuses on the reactive species found in the bulk liquid. Three parts are considered: gas phase, liquid interface (representing the small region near the depression in the liquid, where the radicals are still present, *cf.* Fig. 8A) and bulk liquid. The species are written in boxes of which the thickness indicates the relative density of the species in that phase (gas, liquid interface or bulk liquid). Diffusion from one phase to another is indicated with vertical blue arrow lines, where the thickness represents the fraction of that species that reaches the destination. Chemical reactions are indicated with black arrow lines, and in the liquid interface the thickness is again a measure for the relative contribution of this reaction towards the products. In the bulk liquid, a constant line thickness is used, as the species are typically only produced here *via* 1 or 2 reactions. Reactions with ambient air molecules (O_2, N_2 or H_2O) are included in the figure, but these species are not depicted for the sake of clarity. The equilibrium between HNO_2/NO_2^-, HO_2/O_2^- and $ONOOH/ONOO^-$ is included in the reaction set (see Table S2 in the ESI†) and these species are considered together, but for the sake of clarity, the species are only indicated here by their deprotonated form, which has the highest density (*cf.* Fig. 9).

 This journal is © the Owner Societies 2018

contrast to the density of, *e.g.*, H_2O_2, which reaches 1.3×10^{15} cm^{-3} (*cf.* Fig. 9).

In Fig. 10, chemical reactions are depicted by black arrow lines. In the liquid interface, the thickness indicates the relative importance of that reaction for the reaction products, while in the bulk liquid, a constant line thickness is used, as typically only one or two reactions contribute to the production of reactive species.

It is clear from Fig. 10 that the production of H_2O_2, HNO_2/NO_2^- and NO_3^- is driven by OH, NO and NO_2 in the liquid interface, besides of course solvation of the gas phase species (*cf.* the high Henry's constants). The most important reactions are reactions 71, 81 and 85 of Table S2 (ESI†), consuming a large part of OH, NO and NO_2 for the production of H_2O_2, HNO_2 and even NO_3^-. These three reactions together contribute up to 99% of the total production of H_2O_2, HNO_2/NO_2^- and NO_3^- at the depression (interface) in the liquid, besides solvation of the gas species.

$$OH + OH \rightarrow H_2O_2 \quad (71)$$

$$NO + OH \rightarrow HNO_2 \quad (81)$$

$$NO_2 + NO_2 + H_2O \rightarrow HNO_2 + NO_3^- + H^+ \quad (85)$$

In addition, OH is not only responsible for the production of H_2O_2 and HNO_2/NO_2^-, but it also leads to partial decomposition of H_2O_2 in the liquid interface, forming HO_2 (reaction 75 in Table S2, ESI†), as well as to partial decomposition of NO_2^-, forming NO_2 and OH^- (reaction 76 in Table S2, ESI†).

$$OH + H_2O_2 \rightarrow H_2O + HO_2 \quad (75)$$

$$OH + NO_2^- \rightarrow OH^- + NO_2 \quad (76)$$

The increasing NO_2 concentration by reaction 76 in turn leads to an increase in the production of NO_2^- and NO_3^- through reaction 85. The above five reactions, *i.e.*, 71, 75, 76, 81 and 85, constitute the most important processes found in the liquid interface, eventually generating H_2O_2, HNO_2/NO_2^-, NO_3^- and HO_2/O_2^-.

This picture changes significantly in the bulk liquid, where H_2O_2 is generated by the self-decomposition of HO_2/O_2^- (reaction 77 in Table S2, ESI†), while NO_3^- is mostly produced by the reaction between O_3 and HNO_2/NO_2^- (reaction 70 in Table S2, ESI†). Unlike H_2O_2 and NO_3^-, the other species, *i.e.*, HNO_2/NO_2^-, HO_2/O_2^- and O_3 are generated in the bulk solely through diffusion and convection from the liquid interface, and are not formed *via* chemical reactions (due to the absence of the required short-lived species). However, HO_2/O_2^-, O_3 and HNO_2/NO_2^- are involved in both reactions 77 and 70, which form the main loss processes for these species in the bulk liquid.

$$HO_2 + H_2O + O_2^- \rightarrow O_2 + H_2O_2 + OH^- \quad (77)$$

$$NO_2^- + O_3 \rightarrow O_2 + NO_3^- \quad (70)$$

O_3 in the liquid mostly originates from the reaction between O and O_2, as transfer from the gas phase is limited by a low Henry's constant. In turn, O_3 is mainly involved in reaction 70 towards the formation of NO_3^- (*cf.* Fig. 10), both in the liquid interface and in the bulk liquid, as already stated above. Although this reaction is the major loss process for O_3, it contributes very little to the total production of NO_3^- in the liquid interface, where reaction 85 is much more important. Furthermore, despite being among the most pronounced reactions in the bulk liquid, the rate of reaction 70 is still very low, which explains the relatively slow changes in the density of O_3 in the bulk as a function of time (*cf.* Fig. 8).

Next to H_2O_2, NO_2^-, O_3 and NO_3^-, O_2^- is also observed in the bulk, albeit at significantly lower concentrations (*cf.* Fig. 9). Like H_2O_2, the accumulation of O_2^- in the liquid results from the combination of solvation (as HO_2 also has a high Henry's constant) and the presence of OH in the liquid interface, which can react with H_2O_2 forming HO_2 *via* reaction 75 (see above). On the other hand, OH can also react with HO_2/O_2^-, forming O_2 *via* reactions 73 and 74 (Table S2, ESI†). Both reactions 73 and 74 are found to be the main loss processes for HO_2/O_2^- in the liquid interface (not depicted in Fig. 10).

$$OH + HO_2 \rightarrow H_2O + O_2 \quad (73)$$

$$OH + O_2^- \rightarrow OH^- + O_2 \quad (74)$$

Despite the presence of several production reactions for solvated O_2^-, its density in the liquid remains low (not exceeding 10^{13} cm^{-3}, *cf.* Fig. 9), due to the presence of NO in the liquid interface (*cf.* Fig. 8A) leading to the formation of ONOOH/$ONOO^-$ (reaction 83 in Table S2, ESI†). In the bulk, however, the self-decomposition of O_2^-/HO_2 becomes the most important loss process, forming H_2O_2 *via* reaction 77 (see above), and to a lesser extent by reaction 92 (due to the lower concentration of HO_2 in a solution with pH 7.3).

$$NO + HO_2 \rightarrow ONOOH \quad (83)$$

$$HO_2 + HO_2 \rightarrow O_2 + H_2O_2 \quad (92)$$

Finally, ONOOH/$ONOO^-$ is mainly formed in the liquid interface from OH and NO_2, *via* reaction 84. However, given the fast solvation of ONOOH from the gas phase to the liquid phase (*cf.* high Henry's constant), we expect that ONOOH generated in the gas phase will also contribute to its liquid density, but due to a lack of sufficient data in the literature, the gas phase chemistry of ONOOH could not be included in this model. The liquid chemistry changes in the bulk, where reaction 78 forms the main production source for ONOOH/$ONOO^-$, albeit at a much slower rate. However, the latter will increase with increasing acidity.[70]

$$NO_2 + OH \rightarrow 0.7(NO_3^- + H^+) + 0.3(ONOOH) \quad (84)$$

$$H_2O_2 + NO_2^- + H^+ \rightarrow ONOOH + H_2O \quad (78)$$

On the other hand, ONOOH also decomposes into NO_3^- (reaction 89). Because of this, combined with reactions 90 and 91, the concentration of ONOOH remains very low in the liquid (not exceeding 2×10^{10} cm^{-3}) and is found to decrease as a function of time, as explained above (*cf.* Fig. 9). This is

consistent with experimental observations at neutral pH, where ONOOH/$ONOO^-$ is stated to be unstable in solution, forming among others NO_3^-.[72,73]

Thus, OH, NO and NO_2 are formed in the bulk liquid, and quickly react with other species found in the solution to generate long-lived species like H_2O_2, HNO_2/NO_2^- and NO_3^-, and decompose O_3 in the investigated solution. Moreover, the generation of these short-lived species (OH, NO and NO_2) is expected to contribute to the oxidation of biomolecules found in the treated solution.[70,74]

$$ONOOH \rightarrow NO_3^- + H^+ \quad (89)$$

$$ONOOH \rightarrow OH + NO_2 \quad (90)$$

$$ONOO^- \rightarrow NO + O_2^- \quad (91)$$

In summary, our model predicts that the long-lived species (*i.e.*, H_2O_2, HNO_2/NO_2^-, ONOOH/$ONOO^-$, O_3 and NO_3^-) are mainly generated in the liquid interface, through either solvation from the gas phase, as well as reactions governed by OH, NO and NO_2 originating from the gas phase. Furthermore, these long-lived reactive species accumulate in the bulk liquid as a result of diffusion and convection from the liquid interface. Chemical reactions in the bulk liquid are found at significantly lower rates, and they favor the production of both H_2O_2 and NO_3^-. While H_2O_2 is solely produced by the self-decomposition of HO_2/O_2^- in the bulk liquid (in addition to the transport from the liquid interface), our calculations reveal that the production of NO_3^- is favored in the presence of HNO_2/NO_2^- through the interplay between either H_2O_2 and HNO_2/NO_2^- (with ONOOH/$ONOO^-$ as intermediate) or O_3 and HNO_2/NO_2^-.

The results presented in this work of course depend on the simulated working conditions, such as the treatment gap, flow rate and pH of the treated liquid. Decreasing the flow rate and/or increasing the gap leads to a significant increase in the time needed for the plasma species to come in contact with the liquid interface, which has an impact on the simulated chemistry. As a result, the short-lived gas species (*i.e.*, O, N, OH, HO_2 and NO_3) will have more time to be consumed towards the formation of the long-lived gas species (*i.e.*, H_2O_2, O_3, HNO_2 and HNO_3). This will lead to a decrease in the density of the short-lived gas species and an increase in the density of the long-lived gas species, at the liquid interface, with decreasing flow rate and/or increasing gap. This, in turn, will greatly influence the observed liquid chemistry at the liquid interface (*cf.* Fig. 10). Indeed, a lower density of short-lived liquid species at the interface will result in lower reaction rates for the formation of the long-lived liquid species. The decrease in formation of long-lived liquid species at the liquid interface will, however, be compensated by the higher density of long-lived gas species that come in contact with the liquid interface, as mentioned above. Simultaneously, a lower gas velocity also influences the number of species that is introduced in the system per unit of time. Combined, the number of reactive species inside the liquid will decrease with decreasing flow rate.

Furthermore, as the concentration of H^+ and OH^- has a significant impact on the simulated chemistry, due to equilibrium of weak acids, pH dependent reactions and reactions with either H^+ or OH^-, the pH of the solution will play a crucial role in the results observed in this work. On one hand, as H_2O_2 and HNO_2/NO_2^- are known to form ONOOH/$ONOO^-$ at decreasing pH values,[70] we expect a slow decrease of these reactive species, eventually forming NO_3^- (through ONOOH/$ONOO^-$ as the intermediate)[70] and decreasing the activity of the produced PTL as a function of time, as was indeed observed in the experiments.[70] On the other hand, a decrease in the ozone density in solution with increasing pH can be expected. This is, first of all, caused by the increasing importance of the peroxone chemistry at high pH values (reaction 93 of Table S2, ESI†). Additionally, we expect that reactions with OH^- and NO_2^- will become more important with increasing pH (reactions 69 and 70 of Table S2, ESI†), leading to the further consumption of ozone in solution.

We plan to extend our model in the near future, to be able to investigate the effect of different working conditions (flow rate, gap, liquid volume and pH) on the liquid chemistry and on the accumulation of reactive species in more detail. In addition, we plan to evaluate the behavior after plasma treatment (*i.e.*, no inlet velocity and plasma species densities), for the evolution of the species in the produced PTL at longer timescales, and to investigate the stability of the PTL after plasma treatment.

Conclusions

We have developed a 2D axisymmetric fluid dynamics model to investigate the plasma jet–liquid interactions for an Ar plasma jet, focusing in particular on the accumulation and chemical reactions of plasma generated reactive species in a buffered aqueous solution, as well as transport from the gas phase. 20 gas phase species and 22 liquid phase species are included, which react in 57 gas phase reactions and 42 liquid phase reactions. Furthermore, transport of the plasma species from the gas phase to the liquid, governed by Henry's law, as well as water evaporation, is taken into account. Our results indicate that the flow pattern in the liquid depends on the velocity of the effluent, which is determined by the gap and the gas flow rate. Due to the high gas phase velocity, we observed the generation of a reverse vortex in the liquid, which relocates towards the gas–liquid interface with increasing velocity. This results in a complex flow pattern at the liquid interface, which affects the chemistry in the liquid. Indeed, due to the liquid flow pattern, short-lived reactive species will remain close to the interface and cannot reach the bulk liquid. The observed liquid flow pattern also leads to the accumulation of long-lived reactive species, *i.e.*, H_2O_2, HNO_2/NO_2^-, NO_3^-, O_3, HO_2/O_2^- and ONOOH/$ONOO^-$, as well as NO and NO_3, in the reverse vortex situated at the border of the liquid vessel.

As the short-lived reactive species are consumed at the interface, generating long-lived reactive species, they are not encountered in the bulk liquid. Indeed, our results show that

 This journal is © the Owner Societies 2018

only H_2O_2, HNO_2/NO_2^-, NO_3^-, O_3, HO_2/O_2^- and ONOOH/$ONOO^-$ are present in the bulk liquid during plasma treatment. Furthermore, from these results we can expect that only H_2O_2, HNO_2/NO_2^- and NO_3^- will remain in the liquid after plasma treatment, consistent with experimental observations.[70,71] The other species found in the bulk liquid, *i.e.*, O_3, HO_2/O_2^- and ONOOH/$ONOO^-$, are consumed in the liquid chemistry. Indeed, O_3 is consumed by the reaction with HNO_2/NO_2^-, while HO_2/O_2^- and ONOOH/$ONOO^-$ decompose to form either H_2O_2 or both HNO_2^-/NO_2^- and NO_3^-, respectively.

In this work, we have presented the model for a specific set of treatment conditions, so it should be kept in mind that the presented results are only valid for these conditions. As the calculated chemistry and the presented results depend on the treatment conditions, we plan to extend the presented model in the future, to be able to assess the impact of various working conditions (flow rate, gap, volume and pH) on the simulated accumulation of reactive species, in order to support and explain experimental data.

Finally, it should be noted that the simulations presented here were performed only while the plasma jet was turned on. This means that a continuous flow of new species was introduced during the simulations. Because of this, our simulations can provide no conclusion yet on the stability of the simulated PTLs after plasma treatment. However, we are currently investigating the latter, as indeed, switching off the plasma will have an impact on the liquid flow, and therefore on the further accumulation of species. Hence, in the near future we plan to evaluate the PTL behavior after plasma treatment (*i.e.*, no inlet velocity and plasma species densities), to investigate the evolution of the species in the produced PTL, and more in general, the stability of the PTL, after plasma treatment.

We believe that our study provides valuable insight into the interaction of a plasma jet with liquid water, for the generation of plasma treated liquids, as well as more generally for plasma medicine.

Computational setup

General processes described in the model

We developed a two-dimensional axisymmetric fluid dynamics model in COMSOL Multiphysics™ version 5.0. Our model combines three physical modules: (i) transport of momentum, governed by the incompressible and time-independent Navier-Stokes equations, (ii) transport of heat, controlled by the principle of conservation of energy, and (iii) transport of mass, which is affected by diffusion and convection.

These three modules are calculated separately for both the gas and liquid phase. However, they are coupled to each other through the gas–liquid interface. Although no inlet or initial velocity is defined in the liquid, the liquid flow is coupled with the gas flow through a drag force implemented at the gas–liquid interface. This results in a shear stress in the liquid from the gas flowing over the interface. In addition, transport of heat is considered to be continuous over the interface and governed by the properties of the respective phase (*i.e.*, air and water). Transport of species over the interface is controlled by Henry's law. Finally, the evaporation of water is implemented at the interface, as well as the heat of evaporation. More details about the governing equations in the model can be found in the ESI.†

We describe four major processes: (i) transport of species in the gas and liquid phase, by both diffusion and convection, (ii) gas and liquid phase chemistry, (iii) transport of species over the gas–liquid interface and (iv) transport of heat, affecting both the chemistry and the transport of species. Combining all these processes in a fully coupled simulation, able to describe time-scales up to minutes as used in experimental treatments, results in a computationally highly demanding model. For this reason, we do not simulate the active discharge of the plasma itself, and we only consider the afterglow of the plasma. Indeed, when simulating a discharge, very fast processes have to be taken into account (like electron impact reactions), which hinders the calculations of the model for the envisioned time-scales (*i.e.*, minutes). However, in order to obtain reliable results, we use results from 0D plasma chemical kinetics models,[56,60] which describe the plasma discharge for a plasma jet in great detail, as an input for our model. This is explained in the ESI† (see Table S1).

The absence of a plasma discharge or an electric field in the effluent might affect the flux of reactive species in the plasma effluent. However, we expect that this influence will have no significant impact on the results for three reasons. Firstly, the discharge could in principle result in heating of the gas, influencing the momentum of the gas molecules. This could be coupled back to the inlet flow. Although we only simulate the effluent, we take into account the increase in temperature as a result of the plasma discharge, for the calculations of both the gas flow and the gas chemistry (see below). However, this effect turns out to be minor. Secondly, the plasma species are influenced by the discharge and electric fields, but the majority of the flow consists of neutral gas species, which will not be affected by the plasma. Finally, the electric field could have an impact on the momentum of certain plasma species, which could enhance the flux of species in the effluent. However, this only holds true for devices with a significant electric field in the effluent.

Simulated system

The geometry used in this investigation is illustrated in Fig. 11, and represents a plasma jet powered by a pin electrode, such as the kINPen. The physical and chemical properties of this plasma jet, as well as its biological impact, have been widely studied, and it has also been used already for clinical treatment[57,62] as mentioned above. This plasma source consists of two electrodes, *i.e.*, a central pin electrode with a diameter of 1 mm surrounded by a grounded electrode with an inner diameter of 1.6 mm. The dimensions of the simulated liquid vessel are 7 cm × 3.5 cm, leading to a volume of around 135 mL. We assume that the liquid vessel is not filled to the very top during experimental treatment. As such, a wall with a height of 0.5 cm is introduced at the end of the liquid interface,

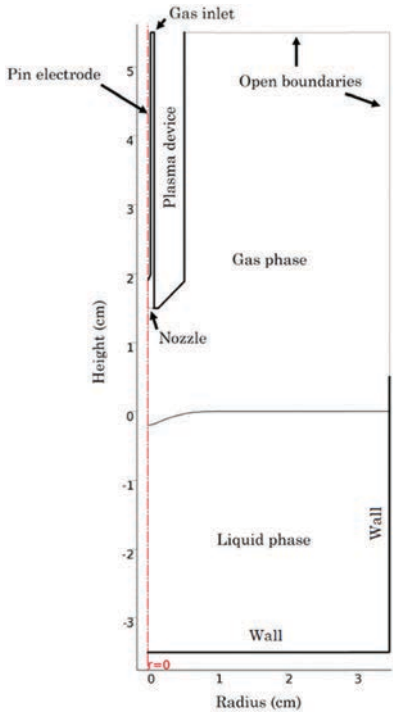

Fig. 11 Schematic picture of the geometry used in the model. The geometry is represented by an axisymmetric 2D model (symmetry axis at r = 0, located at the center of the plasma jet).

mimicking the top border of the liquid container. During the simulations, treatment in open air is assumed, which is implemented using open boundaries in the gas phase.

A treatment gap of 15 mm was chosen, because experimental results with the kINPen IND showed an active discharge at the liquid surface for smaller treatment gaps,[75] which significantly affects the liquid chemistry. As the plasma discharge itself is not simulated here, a larger treatment gap (*i.e.*, 15 mm) is used. The general parameters of the geometry are listed in Table 1. We consider a 2D axisymmetric model, and the symmetry axis is situated at the center of the plasma jet. As such, the full geometry can be obtained by rotating the 2D image of Fig. 11 around the red line at r = 0. Because of the high velocity of the plasma jet (*i.e.*, maximum velocity of 72.8 m s^{-1} at a gas flow rate of 3 slm; see Results and discussion), a depression in the surface is often observed experimentally.[63,64] The depth and width of this depression are highly dependent on the treatment conditions and the plasma jet used. Due to lack of detailed information, we set the depression in our model to 2 mm deep and 9 mm wide (*cf.* Fig. 11).

We consider a buffered solution at pH = 7.3. To achieve this, the concentration of H^+ and OH^- are kept fixed and are determined by the applied pH value. We assure that charge neutrality of the liquid is preserved, in spite of the fact that more negative ions are present, due to the pH used and the liquid chemistry (see below). Indeed, we assume that positive counter ions, which are responsible for the preservation of charge balance (*e.g.*, K^+ or Na^+), do not take part in chemical reactions with the reactive species. Therefore, they are not included in the liquid chemistry in this model.

Fluid flow

We use the time-independent Navier–Stokes equations in our model. These equations are solved until a steady-state is reached, after which the steady-state velocity profile is used as the input for the time-dependent calculations of the convection–diffusion equations for heat and mass transport (see below). This approach is justified as the feed gas of the plasma device is typically already flowing prior to the discharge. In this model, a flow rate of 3 slm (standard liters per minute) is used. As the hydraulic diameter of the nozzle is 1.6 mm, this yields a gas flow velocity of 72.8 m s^{-1}, and thus a Reynolds number of *ca.* 3500 is obtained, resulting in a turbulent gas flow. Therefore, the flow in the gas phase is calculated using the Reynolds-averaged Navier–Stokes equations (RANS) for an incompressible flow in air at 1 atm. For this purpose, the k-ε turbulence model, as built in COMSOL Multiphysics, is utilized. This is a widely used and well-established model for the description of a turbulent fluid flow. More details can be found in ref. 65. On the other hand, the maximum velocity of the liquid is typically much lower than that of the gas, *i.e.*, 10.4 m s^{-1} in our model. Therefore, a laminar behavior is expected and introduced in the water phase.

Transport of heat

The initial temperature of both the gas and liquid phase is set to 293 K. However, as a plasma jet is typically characterized by a higher gas temperature, the temperature of the inflowing gas and the walls inside the plasma jet device is set to 327 K, corresponding to the gas temperature reported in ref. 56 and 66. Indeed, as the active discharge is not simulated, the temperature corresponding to this discharge is implemented with the inflowing gas. To assure that the gas at the nozzle has a temperature of 327 K, the walls inside the plasma device are kept at this temperature as well. All the other walls in the model are considered to be isolating, except for the gas–liquid interface, where a continuous heat flow from the gas to the liquid is assured.

Chemistry and transport of species

We assume treatment in ambient air (78.09% N_2, 20.95% O_2 and 0.96% H_2O) with a pressure of 1 atm. The gas phase and

Table 1 Dimensions and working conditions used in the model

Inner diameter of plasma jet	1.6 mm
Diameter of pin electrode	1 mm
Dimensions of water vessel	7 cm diameter; 3.5 cm height
Volume liquid	135 mL
Flow rate at inlet of plasma jet device	3 slm
Gap between nozzle of plasma jet device and liquid surface	15 mm

This journal is © the Owner Societies 2018

Table 2 Gas phase and liquid phase species included in the model

	Gas phase species	Liquid phase species
Radicals	O, OH, HO_2, N, NO, NO_2, NO_3, H	O, OH, HO_2, NO, NO_2, NO_3, H
Excited species	$O_2(a)$ ($^1\Delta_g$)	
Molecules	H_2, O_2, O_3, H_2O, H_2O_2, N_2, ONOOH, HNO_2, HNO_3, N_2O_5, Ar	H_2, O_2, O_3, H_2O, H_2O_2, N_2, ONOOH, HNO_2, N_2O_5
Ions		H^+, O_2^-, OH^-, NO_2^-, NO_3^-, $ONOO^-$

liquid phase species considered in our model are listed in Table 2. They are known to be either biologically active or act as precursors for biologically relevant reactive oxygen and nitrogen species (RONS). Furthermore, they are based on the results obtained from the 0D model of Van Gaens and Bogaerts.[60] In that model, 85 different gas phase species and 1928 different chemical reactions were included, which is not feasible in this 2D fluid model, certainly when describing plasma treatment times of several minutes. Therefore, we include here only the most important RONS and corresponding reactions, as reported in ref. 60. This results in 20 gas phase species and 22 liquid phase species (see Table 2). Both sets of species include molecules (long-lived species) as well as radicals and excited species (short-lived species). One of the long-lived species in the gas phase is Ar, because the plasma jet operates with Ar, which flows in humid air, forming various RONS, as well as H-containing species. As ions do not play a significant role in the chemistry of the plasma effluent, as calculated by the 0D simulations, they are not considered in the gas phase in our model (*cf.* Table 2). Furthermore, $O_2(a)$ ($^1\Delta_g$) is included as excited species in the gas phase, as it contributes significantly to the production of biologically relevant species in the effluent.[60,61] However, given the limited knowledge on the liquid chemistry, it could not be included in the liquid phase.

As the liquid phase is kept at a pH of 7.3, we assume that HNO_3, as a strong acid, is deprotonated as soon as it enters the liquid; hence it only occurs in our liquid model in its deprotonated form, NO_3^-. For the weak acids (*i.e.*, HNO_2, HO_2 and ONOOH), equilibrium processes are introduced based on their pK_a values (being 3.4, 4.88 and 6.8, respectively), so that the balance between the protonated and deprotonated form is maintained in the liquid, as governed by the pH.

Besides the 20 gas phase species and 22 liquid phase species, a set of 57 gas phase and 42 liquid phase reactions is considered. The set of reactions in the gas phase is a combination of the most important reactions reported by Van Gaens and Bogaerts and by Schmidt-Bleker *et al.*[56,60] for an Ar plasma jet flowing in humid air. However, these models were only for the gas phase (active discharge plasma and afterglow). Given the limited data available in the literature on liquid reactions and reaction rate coefficients for this system, only a small liquid phase reaction set can be used. We adopted the reaction set as used by,[67] but we extended it using the NIST database for kinetics in solution.[68] A full list of the reactions included in the model for both the gas and liquid phase, along with their reaction rate coefficients, can be found in the ESI† (Table S2).

Besides the chemical reactions between the species, the concentration profiles of the various species are also determined by diffusion and convection. Convection is governed by the gas or liquid velocity profile, as calculated by the Navier-Stokes equations (*cf.* section Fluid flow above), while diffusion is dependent on the diffusion coefficients of the species in both the gas and liquid phases. These values are listed in Table S3 in the ESI.† Likewise, the transport of the reactive species between the gas and liquid phase is controlled by Henry's law, stating that the densities of the gas and liquid species are in equilibrium at the interface. This equilibrium is based on Henry's constants for each individual reactive species, which are summarized in Table S3 in the ESI.†

Conflicts of interest

There are no conflicts to declare.

Acknowledgements

The authors thank Petr Lukès (Institute of Plasma Physics AS CR, Czech Republic) and Yury Gorbanev (UAntwerp, group PLASMANT) for the fruitful discussions regarding the chemistry in the model and the plasma–liquid interactions.

References

1 A. Kramer, *et al.*, Suitability of tissue tolerable plasmas (TTP) for the management of chronic wounds, *Clin. Plasma Med.*, 2013, **1**, 11–18.
2 S. Emmert, *et al.*, Atmospheric pressure plasma in dermatology: Ulcus treatment and much more, *Clin. Plasma Med.*, 2013, **1**, 24–29.
3 C. A. J. van Gils, S. Hofmann, B. K. H. L. Boekema, R. Brandenburg and P. J. Bruggeman, Mechanisms of bacterial inactivation in the liquid phase induced by a remote RF cold atmospheric pressure plasma jet, *J. Phys. D: Appl. Phys.*, 2013, **46**, 175203.
4 G. Isbary, *et al.*, A first prospective randomized controlled trial to decrease bacterial load using cold atmospheric argon plasma on chronic wounds in patients, *Br. J. Dermatol.*, 2010, **163**, 78–82.
5 S. U. Kalghatgi, *et al.*, Mechanism of blood coagulation by nonthermal atmospheric pressure dielectric barrier discharge plasma, *IEEE Trans. PLASMA Sci.*, 2007, **35**, 1559–1566.
6 G. Fridman, *et al.*, Blood Coagulation and Living Tissue Sterilization by Floating-Electrode Dielectric Barrier Discharge in Air, *Plasma Chem. Plasma Process.*, 2006, **26**, 425–442.

7 J. Schlegel, J. Köritzer and V. Boxhammer, Plasma in cancer treatment, *Clin. Plasma Med.*, 2013, **1**, 2–7.

8 V. Miller, A. Lin and A. Fridman, Why Target Immune Cells for Plasma Treatment of Cancer, *Plasma Chem. Plasma Process.*, 2016, **36**, 259–268.

9 M. Ishaq, M. Evans and K. Ostrikov, Effect of atmospheric gas plasmas on cancer cell signaling, *Int. J. Cancer*, 2014, **134**, 1517–1528.

10 X. Lu, G. V. Naidis, M. Laroussi, S. Reuter, D. B. Graves and K. Ostrikov, Reactive species in non-equilibrium atmospheric-pressure plasmas: Generation, transport, and biological effects, *Phys. Rep.*, 2016, **630**, 1–84.

11 J. Golda, *et al.*, Concepts and characteristics of the 'COST Reference Microplasma Jet', *J. Phys. D: Appl. Phys.*, 2016, **49**, 84003.

12 K. Weltmann, *et al.*, Plasma Processes and Plasma Sources in Medicine, *Contrib. Plasma Phys.*, 2012, **654**, 644–654.

13 J. Winter, R. Brandenburg and K. Weltmann, Atmospheric pressure plasma jets: an overview of devices and new directions, *Plasma Sources Sci. Technol.*, 2015, **24**, 64001.

14 J. Ehlbeck, *et al.*, Low temperature atmospheric pressure plasma sources for microbial decontamination, *J. Phys. D: Appl. Phys.*, 2011, **44**, 13002.

15 T. Sato, M. Yokoyama and K. Johkura, A key inactivation factor of HeLa cell, *J. Phys. D: Appl. Phys.*, 2011, **44**, 372001.

16 M. Vandamme, *et al.*, ROS implication in a new antitumor strategy based on non-thermal plasma, *Int. J. Cancer*, 2012, **130**, 2185–2194.

17 T. Adachi, H. Tanaka, S. Nonomura, H. Hara and S. Kondo, Plasma-activated medium induces A549 cell injury *via* a spiral apoptotic cascade involving the mitochondrial – nuclear network, *Free Radical Biol. Med.*, 2015, **79**, 28–44.

18 L. I. Partecke, *et al.*, Tissue tolerable plasma (TTP) induces apoptosis in pancreatic cancer cells in vitro and in vivo, *BMC Cancer*, 2012, **12**, 473–483.

19 J. Duan, X. Lu and G. He, On the penetration depth of reactive oxygen and nitrogen species generated by a plasma jet through real biological tissue, *Phys. Plasmas*, 2017, **24**, 73506.

20 P. Pacher, J. S. Beckman and L. Liaudet, Central Control of Breathing in Mammals: Neuronal Circuitry, Membrane Properties, and Neurotransmitters, *Physiol. Rev.*, 2007, **87**, 315–424.

21 Y. Ryu, *et al.*, Effects of Background Fluid on the Efficiency of Inactivating Yeast with Non-Thermal Atmospheric Pressure Plasma, *PLoS One*, 2013, **8**, 1–9.

22 D. Yan, N. Nourmohammadi, A. Talbot, J. H. Sherman and M. Keidar, The strong anti-glioblastoma capacity of the plasma-stimulated lysine-rich medium, *J. Phys. D: Appl. Phys.*, 2016, **49**, 274001.

23 H. Tanaka, K. Nakamura, M. Mizuno, K. Ishikawa and K. Takeda, Non-thermal atmospheric pressure plasma activates lactate in Ringer's solution for anti-tumor effects, *Nat. Publ. Gr.*, 2016, **6**, 1–11.

24 T. Adachi, A. Kano, S. Nonomura, T. Kamiya and H. Hara, Histone deacetylase inhibitors stimulate the susceptibility of A549 cells to a plasma-activated medium treatment, *Arch. Biochem. Biophys.*, 2016, **606**, 120–127.

25 C. Klinkhammer, C. Verlackt, D. Smilowicz, F. Kogelheide, A. Bogaerts, N. Metzler-Nolte, K. Stapelmann, M. Havenith and J.-W. Lackmann, Elucidation of Plasma-induced Chemical Modifications on Glutathione and Glutathione Disulphide, *Sci. Rep.*, 2017, **7**, 13828.

26 A. Görlach, Reactive Oxygen Species (ROS) and the Cellular Redox State - from Toxicity to Signaling, *Antioxid. Redox Signaling*, 2005, **7**, 1398–1404.

27 G. Bauer, Increasing the endogenous NO level causes catalase inactivation and reactivation of intercellular apoptosis signaling speci fi cally in tumor cells, *Redox Biol.*, 2015, **6**, 353–371.

28 C. Yang, *et al.*, Selective modification of apoB-100 in the oxidation of low density lipoproteins by myeloperoxidase in vitro, *J. Lipid Res.*, 1999, **40**, 686–698.

29 J. Cadet and J. R. Wagner, DNA Base Damage by Reactive Oxygen Species, Oxidizing Agents, and UV Radiation, *Cold Spring Harbor Perspect. Biol.*, 2013, **5**, 1–18.

30 S. Gebicki and J. M. Gebicki, Formation of peroxides in amino acids and proteins exposed to oxygen free radicals, *Biochem. J.*, 1993, **749**, 743–749.

31 N. Gaur, *et al.*, Combined effect of protein and oxygen on reactive oxygen and nitrogen species in the plasma treatment of tissue, *Appl. Phys. Lett.*, 2015, **107**, 103703.

32 S. Kalghatgi, *et al.*, Effects of non-thermal plasma on mammalian cells, *PLoS One*, 2011, **6**, e16270.

33 M. Naïtali, G. Kamgang-youbi, J. Herry, M.-N. Bellon-Fontaine and J.-L. Brisset, Combined Effects of Long-Living Chemical Species during Microbial Inactivation Using Atmospheric Plasma-Treated Water, *Appl. Environ. Microbiol.*, 2010, **76**, 7662–7664.

34 F. Ye, *et al.*, Plasma-activated medium suppresses choroidal neovascularization in mice: a new therapeutic concept for age-related macular degeneration, *Sci. Rep.*, 2014, **5**, 1–7.

35 S. Mohades, M. Laroussi and V. Maruthamuthu, Moderate plasma activated media suppresses proliferation and migration of MDCK epithelial cells, *J. Phys. D: Appl. Phys.*, 2017, **50**, 185205.

36 H. Tanaka, *et al.*, Plasma-Activated Medium Selectively Kills Glioblastoma Brain Tumor Cells by Down- Regulating a Survival Signaling Molecule, AKT Kinase, *Plasma Med.*, 2011, **1**, 265–277.

37 S. Takeda, *et al.*, Intraperitoneal Administration of Plasma-Activated Medium: Proposal of a Novel Treatment Option for Peritoneal Metastasis From Gastric Cancer, *Ann. Surg. Oncol.*, 2017, **24**, 1188–1194.

38 M. J. Traylor, *et al.*, Long-term antibacterial efficacy of air plasma-activated water, *J. Phys. D: Appl. Phys.*, 2011, **44**, 472001.

39 R. Ma, *et al.*, Non-thermal plasma-activated water inactivation of food-borne pathogen on fresh produce, *J. Hazard. Mater.*, 2015, **300**, 643–651.

40 P. J. Bruggeman, *et al.*, Plasma – liquid interactions: a review and roadmap, *Plasma Sources Sci. Technol.*, 2016, **25**, 53002.

41 N. Y. Babaeva and M. J. Kushner, Reactive Fluxes Delivered by Dielectric Barrier Discharge Filaments to Slightly Wounded Skin, *J. Phys. D: Appl. Phys.*, 2013, **46**, 25401.

 This journal is © the Owner Societies 2018

42 N. Y. Babaeva, W. Tian and M. J. Kushner, The Interaction Between Plasma Filaments in Dielectric Barrier Discharges and Liquid Covered Wounds: Electric Fields Delivered to Model Platelets and Cells, *J. Phys. D: Appl. Phys.*, 2014, **47**, 235201.

43 C. Chen, *et al.*, A Model of Plasma-Biofilm and Plasma-Tissue Interactions at Ambient Pressure, *Plasma Chem. Plasma Process.*, 2014, **34**, 403–441.

44 Y. Suda, *et al.*, Computational study of temporal behavior of incident species impinging on a water surface in dielectric barrier discharge for the understanding of plasma – liquid interface, *Jpn. J. Appl. Phys.*, 2015, **54**, 01AF03.

45 W. Tian and M. J. Kushner, Atmospheric pressure dielectric barrier discharges interacting with liquid covered tissue, *J. Phys. D: Appl. Phys.*, 2014, **47**, 165201.

46 A. M. Lietz and M. J. Kushner, Air plasma treatment of liquid covered tissue: long timescale chemistry, *J. Phys. D: Appl. Phys.*, 2016, **49**, 425204.

47 Z. C. Liu, *et al.*, Physicochemical Processes in the Indirect Interaction Between Surface Air Plasma and Deionized Water, *J. Phys. D: Appl. Phys.*, 2015, **48**, 495201.

48 D. X. Liu, *et al.*, Aqueous reactive species induced by a surface air discharge: Heterogeneous mass transfer and liquid chemistry pathways, *Sci. Rep.*, 2016, **6**, 1–11.

49 S. A. Norberg, W. Tian, E. Johnsen and M. J. Kushner, Atmospheric pressure plasma jets interacting with liquid covered tissue: touching and not-touching the liquid, *J. Phys. D: Appl. Phys.*, 2014, **47**, 475203.

50 S. A. Norberg, E. Johnsen and M. J. Kushner, Helium atmospheric pressure plasma jets interacting with wet cells: delivery of electric fields, *J. Phys. D: Appl. Phys.*, 2016, **49**, 185201.

51 A. Lindsay, C. Anderson, E. Slikboer, S. Shannon and D. Graves, Momentum, heat, and neutral mass transport in convective atmospheric pressure plasma–liquid systems and implications for aqueous targets, *J. Phys. D: Appl. Phys.*, 2015, **48**, 424007.

52 S. Bekeschus, A. Schmidt and T. von Woedtke, The Plasma Jet kINPen – A Powerful Tool for Wound Healing Sander, *Clin. Plasma Med.*, 2016, **4**, 19–28.

53 L. Bundscherer, *et al.*, Impact of non-thermal plasma treatment on MAPK signaling pathways of human immune cell lines, *Immunobiology*, 2013, **218**, 1248–1255.

54 J. W. Fluhr, *et al.*, In vivo skin treatment with tissue-tolerable plasma influences skin physiology and antioxidant profile in human stratum corneum, *Exp. Dermatol.*, 2012, **21**, 130–134.

55 K. Wende, *et al.*, Risk assessment of a cold argon plasma jet in respect to its mutagenicity, *Mutat. Res.*, 2016, **798–799**, 48–54.

56 A. Schmidt-Bleker, J. Winter, A. Bösel, S. Reuter and K.-D. Weltmann, On the Plasma Chemistry of a Cold Atmospheric Argon Plasma Jet with Shielding Gas Device, *Plasma Sources Sci. Technol.*, 2016, **25**, 15005.

57 H.-R. Metelmann, *et al.*, Head and Neck Cancer Treatment and Physical Plasma, *Clin. Plasma Med.*, 2015, **3**, 17–23.

58 H.-R. Metelmann, *et al.*, Scar Formation of Laser Skin Lesions after Cold Atmospheric Pressure Plasma (CAP) Treatment: A Clinical Long Term Observation, *Clin. Plasma Med.*, 2013, **1**, 30–35.

59 J. Lademann, *et al.*, Risk assessment of the application of tissue-tolerable plasma on human skin, *Clin. Plasma Med.*, 2013, **1**, 5–10.

60 W. Van Gaens and A. Bogaerts, Reaction Pathways of Biomedically Active Species in an Ar Plasma Jet, *Plasma Sources Sci. Technol.*, 2014, **23**, 1–27.

61 K. Wende, *et al.*, Identification of the Biologically Active Liquid Chemistry Induced by a Nonthermal Atmospheric Pressure Plasma Jet, *Biointerphases*, 2015, **10**, 29518.

62 M. S. Mann, *et al.*, Introduction to DIN-Specification 91315 Based on the Characterization of the Plasma Jet kINPen s MED, *Clin. Plasma Med.*, 2016, **4**, 35–45.

63 J. F. M. Van Rens, *et al.*, Induced Liquid Phase Flow by RF Ar Cold Atmospheric Pressure Plasma Jet, *IEEE Trans. Plasma Sci.*, 2014, **42**, 2622–2623.

64 M. M. Hefny, C. Pattyn, P. Lukes and J. Benedikt, Atmospheric Plasma Generates Oxygen Atoms as Oxidizing Species in Aqueous Solutions, *J. Phys. D: Appl. Phys.*, 2016, **49**, 404002.

65 D. C. Wilcox, *Turbulence Modelling for CFD*, DCW Industries, Inc., 1993.

66 W. Van Gaens, *et al.*, Numerical Analysis of the Effect of Nitrogen and Oxygen Admixtures on the Chemistry of an Argon Plasma Jet Operating at Atmospheric Pressure, *New J. Phys.*, 2015, **17**, 33003.

67 W. Tian, A. M. Lietz and M. J. Kushner, The Consequences of Air Flow on the Distribution of Aqueous Species During Dielectric Barrier Discharge Treatment of Thin Water Layers, *Plasma Sources Sci. Technol.*, 2016, **25**, 55020.

68 NIST Solution Kinetics Database, http://kinetics.nist.gov/solution/.

69 W. Van Gaens and A. Bogaerts, Kinetic Modelling for an Atmospheric Pressure Argon Plasma Jet in Humid Air, *J. Phys. D: Appl. Phys.*, 2013, **46**, 275201.

70 P. Lukes, E. Dolezalova, I. Sisrova and M. Clupek, Aqueous-Phase Chemistry and Bactericidal Effects from Gaseous Plasmas in Contact with Water, *Plasma Sources Sci. Technol.*, 2014, **23**, 15019.

71 P. Girard, *et al.*, Synergistic Effect of H_2O_2 and NO_2 in Cell Death Induced by Cold Atmospheric He Plasma, *Sci. Rep.*, 2016, **6**, 29098.

72 F. Girard, *et al.*, Formation of Reactive Nitrogen SPecies including Peroxynitrite in Physiological Buffer exposed to Cold Atmospheric Plasma, *RSC Adv.*, 2016, **6**, 78457–78467.

73 S. Pfeiffer, *et al.*, Metabolic Fate of Peroxynitrite in Aqueous Solution, *J. Biol. Chem.*, 1997, **272**, 3465–3470.

74 D. B. Graves, Oxy-nitroso shielding burst model of cold atmospheric plasma therapeutics, *Clin. Plasma Med.*, 2014, **2**, 38–49.

75 W. Van Boxem, *et al.*, Anti-cancer capacity of plasma-treated PBS: effect of chemical composition on cancer cell cytotoxicity, *Sci. Rep.*, 2017, **7**, 16478.